THE JOURNAL OF PHYSICAL CHEMISTRY C

Article

pubs.acs.org/JPCC

Near-Field Imaging of Cell Membranes in Liquid Enabled by Active Scanning Probe Mechanical Resonance Control

Kyoung-Duck Park,[†,‡] Markus B. Raschke,[†] Min Jung Jang,[§] Jung Hwa Kim,[§] Beom-Hoan O,[‡] Se-Geun Park,[‡] El-Hang Lee,[‡] and Seung Gol Lee*[,‡]

[†]Department of Physics, Department of Chemistry, and JILA, University of Colorado, Boulder, Colorado 80309, United States

[‡]Department of Information and Communication Engineering and [§]Department of Biological Sciences, Inha University, Incheon 402-751, Republic of Korea

Supporting Information

ABSTRACT: Despite the power of far-field super-resolution microscopies for three-dimensional imaging of biomolecular structures and processes, its application is challenged in dense and crowded samples and for certain surface and membrane studies. Although near-field imaging with its ability to provide intrinsic subdiffraction limited spatial resolution at any optical modality, its application to biological systems has remained limited because of the difficulties of routine operation in liquid environments. Here we demonstrate stable and sensitive near-field scanning optical microscopy (NSOM) in a liquid based on a new mechanical resonance control and an optimization of the tip length, achieving a high quality factor (>2800) force sensing of the near-field probe. Through near-field imaging of the spatial distribution of epidermal growth factor receptors (EGFRs) on the membrane of A431 cancer cells as an example, we reveal nanoscale correlations between surface EGFR and intracellular organelle structures with ~50 nm spatial resolution. The method provides a new avenue for surface imaging in viscous liquid media to complement super-resolution microscopy for studies of biological membranes, nanostructures, and interfaces.

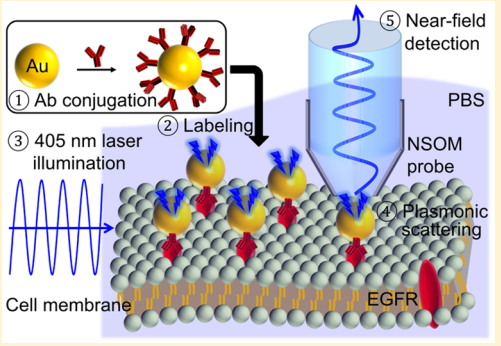

1. INTRODUCTION

Recently, a range of super-resolution fluorescence microscopies have opened the door for studying biomolecular processes with subdiffraction limited spatial resolution. For example, stimulated emission depletion (STED) increases spatial resolution by selectively deactivating fluorophores.[1,2] Likewise, photoactivated localization microscopy (PALM) and stochastic optical reconstruction microscopy (STORM) overcome the diffraction barrier by using photoswitchable fluorescent probes.[3,4]

However, these super-resolution microscopies require not only specific fluorophores optimized for the targets but also low-density labeling to decrease localization uncertainty, limiting spatial resolution and imaging speed.[5,6] In addition, high excitation fluence is needed to obtain the number of photons necessary for accurate position localization of the emitters. Therefore, photobleaching appears to be an unavoidable limiting factor.[7] Also on the basis of a far-field sectioning method, they are not necessarily ideal to investigate nonplanar surface and interfaces (Figure 1a).

Near-field imaging, on the contrary, provides intrinsically diffraction-unlimited spatial resolution and is applicable to essentially any optical modality beyond fluorescence, including linear, inelastic, and nonlinear spectroscopies.[8] Applied with great success to a wide range of material systems, especially with the advent of scattering scanning near-field optical microscopy (s-SNOM),[9−11] it provides single molecule sensitivity, few nanometer spatial resolution, and in the extension to ultrafast spectroscopy, even few-femtosecond temporal resolution.[12,13]

On the one hand limited to surfaces and interfacial regions accessible by the near-field probe, this, on the other hand, can make near-field imaging ideal for the study of membranes and protein nanostructures, with near-field localization profiling the surface thus discriminating against bulk signals (Figure 1b). In addition, on the basis of force-feedback controlling the near-field probe interaction, it provides simultaneous high-resolution topographic information and multimodal imaging of membrane mechanical properties, e.g., viscoelasticity and adhesion force,[14] as well as a wide range of optical modality.

However, a major limitation of near-field imaging for biological applications, has long been the difficulty of operation in liquid environments. Typically, on the basis of scanning probe microscopy (SPM) techniques, several attempts have been made for operation of near-field scanning optical microscopy (NSOM) and tip-enhanced Raman spectroscopy (TERS) in liquid, in particular for the study of cell membranes and electrochemical interfaces.[15−21] However, the near-field

Special Issue: Richard P. Van Duyne Festschrift

Received: July 28, 2016
Published: July 28, 2016

DOI: 10.1021/acs.jpcc.6b06563
J. Phys. Chem. C 2016, 120, 21138−21144

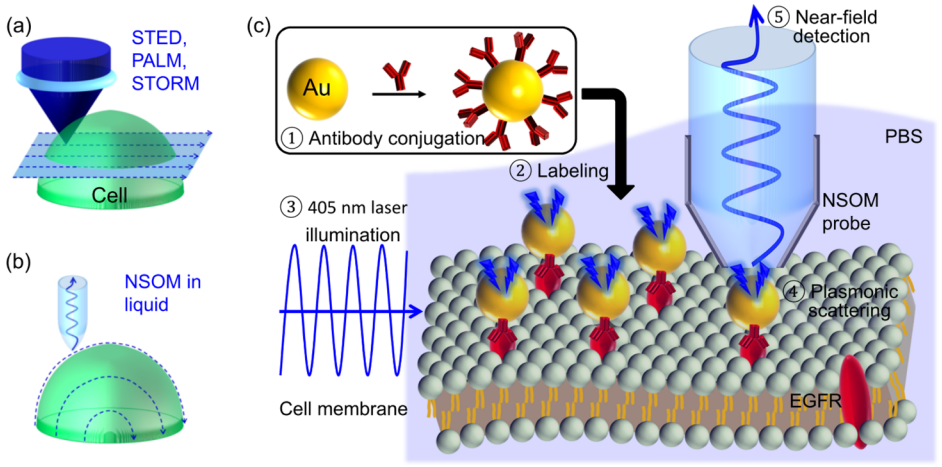

Figure 1. Comparison of optical nanoprobe imaging methods: typical super-resolution microscopy based on far-field sectioning (a) and NSOM based on near-field profiling (b). (c) Procedure for NSOM imaging of EGFRs on the cell membrane in liquid. Anti-EGFRs are conjugated to AuNPs for labeling to the A431 cell membrane. Near-field scattered light from the AuNPs is collected by a NSOM probe under 405 nm laser excitation.

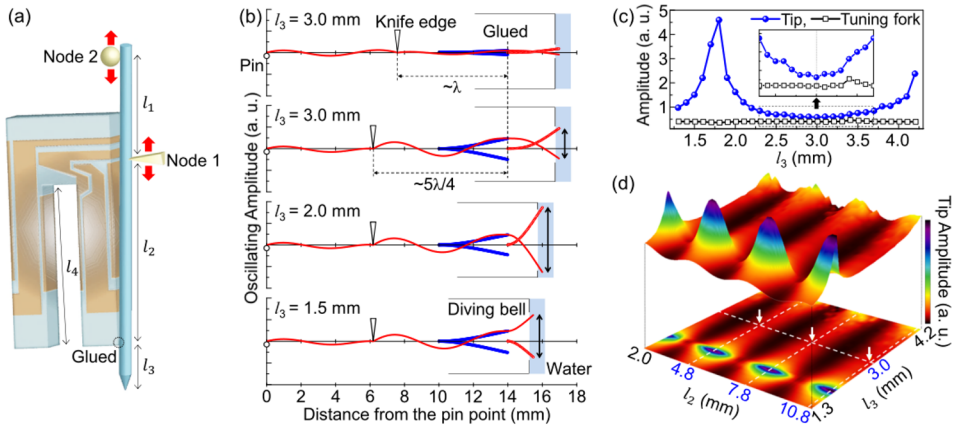

Figure 2. (a) Illustration of high-Q oscillator controlled by introducing two nodes at variable distances. (b) Calculated oscillating amplitudes of the tuning fork (blue lines) and the fiber probe (red line). (c) Calculated amplitude variation of the tuning fork-end (black squares) and tip apex (blue circles) as a function of l_3 while maintaining l_1 = 6.2 mm and l_2 = 7.8 mm. (d) 3D plot of amplitude variation of tip apex as a function of l_2 and l_3.

probe is operated on the basis of a scanning probe force sensor, where its mechanical resonance deteriorates in frequency stability and quality (Q) factor in a liquid medium, sensitive to viscosity, density, and temperature.[22] Yet, with the near-field signal very sensitive to tip−sample distance, high precision and stability in the force-feedback is required to avoid imaging artifacts.

A refined approach for optimal force control in liquid as a basis for advanced near-field imaging of cell surfaces and membrane proteins is thus desired. Here, we demonstrate a new approach of mechanical resonance control of the near-field probe providing stable and sensitive imaging in liquid. It is based on a combination of length and nodal point optimization of the mechanical force sensor (tuning fork/fiber probe assembly) to achieve high Q-factor and sensitive force control in liquid. As an application example, we label gold nanoparticles (AuNPs) to the biomolecules on the cell membrane as nanoplasmonic antennas to overcome the low sensitivity of the nanoapertured near-field probe, as illustrated in Figure 1c. Through high-resolution (~50 nm) near-field imaging of the spatial distribution of epidermal growth factor receptors (EGFRs) on the membrane of A431 cancer cells in liquid, we reveal nanoscale heterogeneity of surface EGFRs, as demonstating experiment representing a typical bioimaging application.

Following the description and characterization of the force sensor design, we show the results of its use in liquid cell membrane imaging and conclude with a short perspective of the approach for a broad range of nanobioimaging applications.

2. EXPERIMENTAL AND THEORETICAL METHODS

Our method is in principle based on established quartz tuning fork shear force sensing to control and scan the near-field probe at and across the cell membrane. However, in a conventional implementation, the Q-factor of the NSOM probe is reduced to <100 when the tip is immersed in liquid. To overcome this probelm, we recently developed a method to control the Q-factor of the quartz tuning fork based NSOM probe, as shown in Figure 2a.[23] In that method, the resonance frequency and the Q-factor of the NSOM probe are controlled by introducing two nodal wedges (node 1, knife edge point; node 2, pinpoint) and adjusting their positions like fingering a guitar. When the positions of the two nodal wedges are optimized, a high Q-factor is achieved because the vibrational energy of the tuning fork is efficiently transferred to the NSOM probe (l_1 and l_2) due to the effective vibration isolation at node 1 (for details on

DOI: 10.1021/acs.jpcc.6b06563
J. Phys. Chem. C 2016, 120, 21138−21144

numerical analysis, see further in this section and the Supporting Information). In addition, we provide a novel physical concept to operate near-field microscopy in a liquid by optimizing the tip length, l_3, to minimize the resistance from liquid viscosity. This optimization is a key enabling step for nanobio imaging applications, and it was not yet discussed in our previously published two nodal wedges method.[23]

Modeling of the High-*Q* NSOM Head. The high-*Q* oscillator is divided into five vibration sections (Figure S1): Rods 1, 2, and 3 corresponding to the fiber probe have lengths of l_1, l_2, and l_3, respectively, and their lengths are adjusted by changing the positions of two nodal wedges. Rods 4 and 5, corresponding to two prongs of the tuning fork, have equal lengths of l_4. The amplitude function for the five sections can commonly be specified with the mathematical expression as $U(l) = a\cos(\beta l) + b\sin(\beta l) + c\exp[\beta(l - l_{in})] + d\exp[\beta(l_{in} - l)]$, where a, b, c, and d are unknown coefficients of the displacement function. The variable l is the distance measured from the base of the tuning fork for rods 4 and 5 and the distance measured from the pinpoint support for other sections. The parameter β is defined as $\beta = \omega^2\rho S/EI$ (ω is a natural frequency, ρ is a density, S is a cross sectional area, E is a Youngs modulus, and I is a moment of inertia) with specific values determined from refs 24 and 25. To suppress numerical error, the initial coordinate l_{in} of each vibrating section is introduced into the exponent of the displacement function.

The system of equations for unknown coefficients is derived by applying boundary conditions to six boundary points (Figure S1). The boundary conditions in tip-end and tuning fork-end are deduced on the basis of the theory for bending vibration of a beam.[26] Other boundary conditions are carefully derived by considering the mechanical properties of each part. Because the system of equations can have nontrivial solutions only when the determinant of the coefficient matrix becomes zero, the frequency having a zero determinant is chosen as a resonance frequency (ω_R) for the high-Q oscillator.

NSOM Setup. A 405 nm laser is used as an excitation source, and the near-field signal is collected using a commercially available Al-coated tapered fiber having an aperture diameter of ∼50 nm and is then converted into an electric signal by a photomultiplier tube (R2027 from Hamamatsu) that is placed at the opposite end of the fiber. The position of the sample is changed using a piezoelectric transducer (PZT, P-611.3 from Physik Instrumente) that has a 0.1 nm resolution; its lateral positions (along the *x*- or *y*-axis) are also scanned using a PZT with a 10 nm position repeatability against a 100 μm total moving range. The height and near-field signal are acquired using an express data acquisition board (PCI-6229 from National Instruments). An office straight pin and a knife edge (cutter) are used as two nodal wedges, and their materials do not play crucial roles in determining resonance characteristics as long as they are sufficiently hard.

Sample Preparation. The EGFRs are labeled with the anti-EGFR antibody conjugated AuNPs. AuNPs are synthesized via a seed-mediated growth method using $HAuCl_4{\cdot}3H_2O$ and trisodium citrate.[27] The synthesized AuNPs have a spherical shape (diameter: ∼30 nm, smaller diameter AuNPs are not used for not reducing scattering intensity). The nanoparticles are diluted in 20 mM 4-(2-hydroxyethyl)-1-piperazineethanesulfonic acid (HEPES) solution (pH = 7.4) and anti-EGFR antibodies are added to another HEPES solution. Then the gold solution is added to the antibody solution with the volume ratio of 10:1 while being stirred. After stirring for 5 min, the solution is left to react for 20 min. The mixture solution is centrifuged at 6000 rpm for 30 min after adding 1% polyethylene glycol (PEG) to prevent aggregation. Then the anti-EGFR conjugated AuNPs are redispersed in PBS buffer solution. The binding mechanism between antibody and AuNP has not been investigated exactly, although it is suggested that the antibody could be adsorbed perpendicularly on the nanoparticle surface at pH = 7.4.[28] Finally, by pouring the anti-EGFR conjugated AuNPs solution onto the surface of A431 cancer cell, an antigen−antibody reaction occurred; i.e., the AuNPs are attached to the EGFRs. The samples are kept at 4 °C for 12 h. After that, the samples are rinsed by PBS buffer solution three times to remove residual AuNPs that are not bound to the EGFR. To confirm the labeling state of the sample, confocal laser scanning microscopy (LSM 510 META, Zeiss) measurement is done using a commercial setup, and the result shows general features of fluorescence imaging (Figure S5). It should be noted that because the AuNPs are coated by PEG and antibody, we believe the prepared cells are nontoxic.[29]

3. RESULTS AND DISCUSSION

Modeling and Simulation. In the following we describe results of mechanical force sensor design and its characterizations. Figure 2b shows simulations of the vibrating amplitude of the oscillators. Because the position of the knife edge (Node 1) corresponds to the node of fiber oscillation, when the length l_2 is $(2n - 1)\lambda_F/4$, where n is an integer and λ_F is the fundamental wavelength given by the natural resonance frequency of the fiber (∼6 mm), the glued point becomes an antinode and has a maximum amplitude owing to the efficient coupled oscillation between the fiber probe and the tuning fork. On the contrary, the glued point becomes a node of the fiber oscillation when l_2 is $n\lambda_F/2$. In this case, the tuning fork loses a significant amount of vibrational energy because the fiber acts as a large damper. Therefore, we set l_2 to $5\lambda_F/4$ to make the high-Q state. Then we compare the amplitudes of the tip-end for different values of l_3 lengths (1.5, 2.0, and 3.0 mm) to find an optimized length (smallest amplitude), which minimizes a damping effect in viscous medium. For the tip oscillation (l_3), the glued point is regarded as the node irrelevant to the l_2 oscillation because the glued point has a boundary condition of partially fixed-end beam, whereas the tip-end has a free-end beam (for details on calculation and interpretation see Figure S2). Accordingly, the position of the antinode of l_3 is about 1.5 mm distant from the point of attachment. Thus, the end of 1.5 and 2.0 mm tips is closer to the antinode and has a large amplitude. On the contrary, the end of 3.0 mm tip is exactly set to the node becaise $\lambda_F/2$ is 3.0 mm; therefore, it has the smallest amplitude.

Figure 2c shows the modeled amplitude variation of tip apex and tuning fork-end as a function of l_3 (l_1 and l_2 are set to 6.2 and 7.8 mm, respectively). Despite the amplitude of the tuning fork terminals for fibers with l_3 = 1.8 mm and l_3 = 3.0 mm being almost identical, the tip-apex amplitude of the l_3 = 1.8 mm tip is ∼9 times larger than the l_3 = 3.0 mm tip due to the antinodal and nodal locations of tip-end from the point of attachment (see Figure S4a for detail). This approach thus provides an optimized length of the tip (l_3) to maximize the force sensitivity when the NSOM measurement is performed in a liquid by minimizing the resistivity of tip vibration to the viscous medium damping.

DOI: 10.1021/acs.jpcc.6b06563
J. Phys. Chem. C 2016, 120, 21138−21144

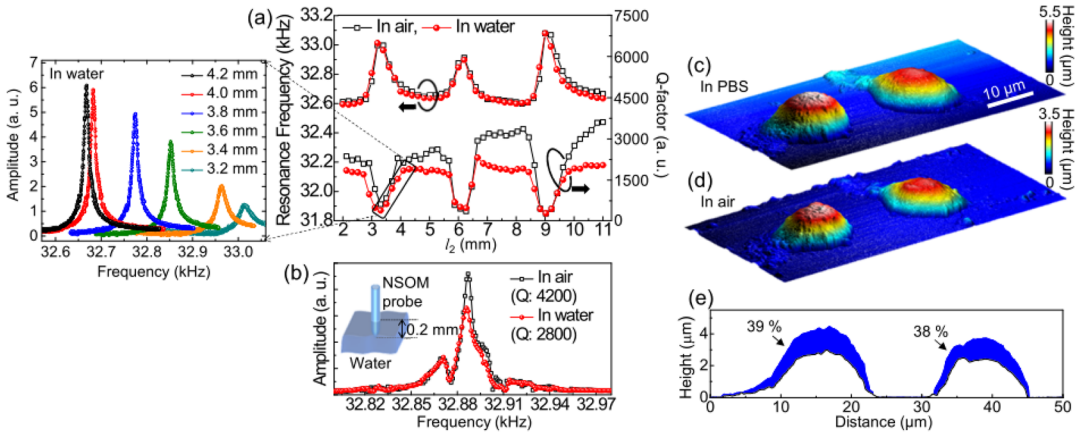

Figure 3. (a) Measured variation of resonance frequency and *Q*-factor of oscillator with respect to the length l_2 while maintaining $l_1 + l_2$ to be 13.6 mm and l_3 to be 3.0 mm, whose tip is exposed to air (black squares) and partially dipped into water (red circles), respectively. Several frequency response curves derived from (a) as an example (left). (b) Frequency response curves for the high-Q oscillator exposed to air (black squares) and partially dipped into water (red circles). Measured topographies of A431 cancer cells being immersed in PBS (c) and exposed to air (d). (e) Their cross-sectional line profiles. The blue area is the volume contraction of cells due to evaporation of water by 39% and 38%.

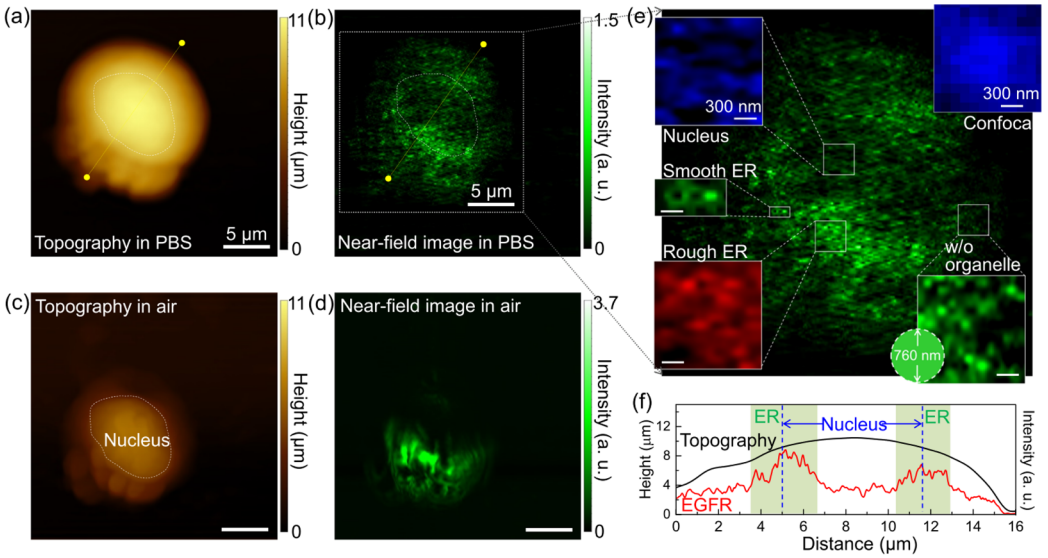

Figure 4. Topography and EGFR distribution on the membrane of the A431 cell. Topography (a) and NSOM image (b) of the A431 cell immersed in PBS, and topography (c) and NSOM image (d) of the A431 cell in air after evaporation of PBS. (e) Local variation of surface EGFR distribution corresponding to intracellular nucleus, rough endoplasmic reticulum (ER), smooth ER, and normal region without organelle. The confocal laser scanning microscope image is derived from Figure S5a. (f) Line profiles of topography and EGFR distribution derived from (a) and (b), which show the density distribution of EGFR on the membrane depend on intracellular organelle composition.

Figure 2d shows amplitude variation of tip apex as a function of l_2 and l_3. The operating condition of NSOM in a liquid environment is optimized by making the highest *Q*-factor with l_2 length (4.8, 7.8, or 10.8 mm) and smallest liquid damping with l_3 length (3.0 mm).

Performance of NSOM Probe in Liquid. To confirm the resonance tunability with the two nodal wedges in liquid, we further study the vibrational characteristics of the NSOM probe experimentally. Figure 3a shows the variation of the resonance frequency and the *Q*-factor as a function of l_2 while maintaining $l_1 + l_2$ constant ($l_1 + l_2$ = 13.6 mm, l_3 = 3.0 mm) for the high-Q NSOM probe exposed to air and partially submerged into water by 0.2 mm. In agreement with the numerical analysis (Figure S2), the resonance frequencies and *Q*-factors change with a 3.0 mm period in l_2, irrespective of the environment (for details on calculation and interpretation see Supporting Information).

Figure 3b shows two frequency response curves measured in air and water under the best fingering condition (l_2 of $3\lambda_F/4$ and l_3 of $\lambda_F/2$). The *Q*-factor defined as the quotient of resonance frequency and the full width at half-maximum (fwhm) of the frequency response maintains a value of 2800 in liquid, which is the highest reported to date. We note that the *Q*-factor of 2800 is also a much higher value than the typical values of a conventional NSOM probe in air. Accordingly, samples immersed in liquid can be measured with as high force sensitivity as in air. The very high *Q*-factor is necessary for and allows for sensitive tip−membrane distance control in liquid even for the soft normal cells (in general, the surface of a cancer cell is harder than that of a normal cell). For the low *Q*-factor NSOM probes (lower than ∼1000 in liquid for 3 mm of tip length), the shear-force feedback is unstable and the cells are usually damaged during scanning. Figure 3c shows the resulting performance in shear force imaging of A431 cells immersed in

DOI: 10.1021/acs.jpcc.6b06563
J. Phys. Chem. C 2016, 120, 21138−21144

PBS, followed by imaging in air (Figure 3d) after evaporation and corresponding volume decrease.

Near-Field Imaging of Cell Membranes. To enhance the optical sensitivity of the NSOM probe for biomolecular imaging on the cell membrane, plasmon labeling by anti-EGFR conjugated AuNPs attached to the EGFRs is used (see Experimental and Theoretical Methods for detail). AuNPs are excited by 405 nm laser illumination to enhance the Rayleigh scattering intensity (scattering intensity $\propto 1/\lambda^4$), and the plasmonic scattering signal is collected through the aperture of an optical fiber probe.

Figure 4 shows the resulting topography (a) and near-field intensity image (b) of a A431 cell measured in PBS. Several textural features can be identified and distinguished with the EGFR distribution and its local density on the cell membrane possibly related to intracellular organelle locations and stuctures. In general, the axial resolution of NSOM is <10 nm due to the exponential decrease of locally confined light intensity with increasing distance to the aperture of NSOM probe.[30] Because the thickness of membrane is 7.5−10 nm and the EGFR resides only on the membrane, Figure 4 does not show the intracellular image but an EGFR distribution within the membrane, correlated only to the extent of intracellular organelles.

It appears that a lower local density of surface EGFR is observed associated with location of cell nucleus. The high-density EGFR region on the membrane is possibly associated with the intracellular endoplasmic reticulum (ER), an especially rough ER, because the main function of rough ER is the synthesis and transport of proteins between the nucleus and cell membrane, and those proteins highly interact with EGFRs.[31] This suggests that the heterogeneous EGFR distribution on the membrane at the zoomed region in red in the left bottom inset corresponds to a structural imprint of an intracellular rough ER region.

On the contrary, the zoomed region of surface EGFRs in the left center in green is suggested to correspond to a structural imprint of the intracellular smooth ER region for several reasons. First, the observed nanoscale mesh structure of surface EGFRs matches well with the well-known structure of smooth ER (see also Figure S6). Second, smooth ER has no ribosomes and functions in lipid metabolism, carbohydrate metabolism, and detoxification.[32] Therefore, EGFRs on the cell membrane have relatively low local density in the region of smooth ER due to the lack of highly interacting molecules.

Despite the EGFR density on the membrane corresponding to a nucleus region being much lower than the membrane region corresponding to the rough ER region (Figure 4f), the cluster diameter is ∼200 nm in both cases, as seen in Figure 4e. Note that from the comparison of the EGFR distribution with the membrane regions on the intracellular nonorganelles, we confirm the cluster size of the nucleus and ER is not limited by the spatial resolution of the near-field probe. In the membrane regions without intracellular organelles, ∼50 nm size spots are resolved, which we believe to be a single or a few EGFRs (see also Figure S7 to verify spatial resolution). The correlation of the heterogeneous EGFR distribution on the cell membrane with intracellular organelle composition implies that some proteins residing at the cell organelles possibly interact with the EGFR on the membrane. In contrast, all these spatial features disappear when the cell is dried, as shown in Figure 4c,d. We guess the observed EGFR distribution in air possibly results from the aggregation of EGFRs due to the volume contraction of cell during evaporation of water.

In previous studies, the ER structure (inside of cell membrane) was visualized to demonstrate the performance of newly developed super-resolution microscopy.[33] Beyond previous super-resolution imagings of organelle structures, our work visualizes the nanoscopic heterogeneneity of membrane biomolecules correlated with intracelluar organelles.

Discussion. There was a considerable body of work to improve the *Q*-factor under aqueous conditions. Rensen et al. reported the *Q*-factor could be improved on the basis of the optimized dipping depth of the NSOM probe ($Q \sim 60$).[34] A similar study was carried out by Lee et al. for imaging soft samples immersed in a liquid ($Q \sim 400$).[35] However, these studies showed limitations in enhancing the *Q*-factor beyond a certain level. Höppener et al. reported a significant *Q* enhancement by attaching a very short fiber probe to a tuning fork and using another optical fiber for laser coupling into the short fiber probe.[30] However, this configuration cannot be applied to a collection-mode NSOM. On the contrary, our method is a versatile tool for collection and illumination modes as well as achieves an extreme *Q*-factor.

In addition to the high *Q*-factor, maintaining a stable resonance condition under aqueous conditions is also significant. Recently, we used the stable resonance zone of fiber probe and the resonance tracking method to overcome the resonance change issue when the immersion depth of the fiber probe is changed due to the evaporating liquid.[22,36] Despite these methods being useful for small area scanning, they are inappropriate to apply to large samples such as biological cells. Thus, we adopt the diving bell structure to maintain a stable resonance condition regardless of liquid evaporation and scanning time.[37]

Recently, several groups achieved reliable near-field fluorescence imaging on the cell membrane under aqueous conditions,[17,38] yet the spatial resolution was limited to ∼100 nm due to the insufficient collection efficiency of the smaller aperture NSOM probes for fluorescence signal. To increase the optical sensitivity and to improve the spatial resolution to ∼50 nm, we label plasmonic AuNPs to the EGFRs on the membrane and measure the Rayleigh scattering instead of the fluorescence signal. This idea is an inverse approach to the use of plasmonic nanostructures at the near-field probe aperture.[19,39] From combinatorial optimization of these requisites, we enable the near-field imaging of biomolecules on the cell membrane under buffered conditions.

Several studies have applied NSOM to the biomolecular imaging of dried cells due to the technical difficulties under buffered conditions.[40−42] However, we believe that cell membrane structures and protein distributions could be deformed due to evaporation of water, as seen in Figure 4. Therefore, NSOM application in liquid environments is highly required for in-depth nanobiology study.

Nowadays, anti-EGFR cancer therapy is widely administered to patients.[43] However, a large portion of patients do not respond to the therapy for unknown reasons. Therefore, better understanding of the complex network of signaling pathways between EGFRs and intracellular biomolecules is required. Fluorescence resonance energy transfer (FRET) and time-resolved spectroscopy have been used to investigate the EGFR mechanisms.[31,44,45] However, these diffraction-limited characterization methods leave many open questions requiring molecular imaging techniques to understand more quantitative

DOI: 10.1021/acs.jpcc.6b06563
J. Phys. Chem. C 2016, 120, 21138−21144

properties. Because the proposed method can be easily combined with other optical modality such as Raman, time-resolved, and absorption spectroscopies,[46−48] we expect the NSOM-FRET or other kinds of combined techniques will be used to explore unexamined nanoscale dynamics on the cell membrane as well as the detailed nanoscale processes.

4. CONCLUSIONS

In summary, we demonstrated a new near-field imaging approach based on the control of the nanomechanical near-field probe resonance by optimizing the tip length of NSOM probe for improved near-field imaging performance in liquid. A very high Q-factor (2800 in water) is achieved by a 3 mm tip as well as two nodal wedges method, and a stable resonance condition is maintained by applying a diving bell structure. To overcome the low optical sensitivity of general fluorescence detection, AuNPs are labeled to the EGFR and the plasmonic scattering signal is probed with ∼50 nm spatial resolution. In the cell membrane imaging of the A431 cell, we reveal the nanoscale correlation between the local distribution of EGFR on the membrane and intracellular organelle composition such as nucleus, rough ER, and smooth ER. The approach is generally applicable for both aperture and scattering type scanning near-field microscopy and TERS, and might lead the way to a greater utility of near-field imaging as a complementary technique to other super-resolution imaging techniques for biological applications in liquid conditions.

■ ASSOCIATED CONTENT

Supporting Information

The Supporting Information is available free of charge on the ACS Publications website at DOI: 10.1021/acs.jpcc.6b06563.

Modeling of high-Q oscillator; supplement of discussion of Figure 3 including additional figures of the oscillator modeling, resonance frequency and Q-factor variation, schematic of the NSOM system, oscillating amplitude curves and test setup photos, laser scanning microscope images, organelle structures, and topographies and NSOM images of A431; and scanning speed of super-resolution microscopy (PDF)

■ AUTHOR INFORMATION

Corresponding Author

*S. G. Lee. E-mail: sglee@inha.ac.kr. Telephone: +82-32-860-7433.

Notes

The authors declare no competing financial interest.

■ ACKNOWLEDGMENTS

This work was supported by the National Research Foundation of Korea Grant funded by the Korean government (MEST) (NRF-2009-0079366).

■ REFERENCES

(1) Hell, S. W.; Wichmann, J. Breaking the Diffraction Resolution Limit by Stimulated Emission: Stimulated-Emission-Depletion Fluorescence Microscopy. *Opt. Lett.* **1994**, *19*, 780−782.

(2) Willig, K. I.; Rizzoli, S. O.; Westphal, V.; Jahn, R.; Hell, S. W. STED Microscopy Reveals That Synaptotagmin Remains Clustered After Synaptic Vesicle Exocytosis. *Nature* **2006**, *440*, 935−939.

(3) Shroff, H.; Galbraith, C. G.; Galbraith, J. A.; Betzig, E. Live-Cell Photoactivated Localization Microscopy of Nanoscale Adhesion Dynamics. *Nat. Methods* **2008**, *5*, 417−423.

(4) Rust, M. J.; Bates, M.; Zhuang, X. Sub-Diffraction-Limit Imaging by Stochastic Optical Reconstruction Microscopy (STORM). *Nat. Methods* **2006**, *3*, 793−796.

(5) Nieuwenhuizen, R. P.; Lidke, K. A.; Bates, M.; Puig, D. L.; Grünwald, D.; Stallinga, S.; Rieger, B. Measuring Image Resolution in Optical Nanoscopy. *Nat. Methods* **2013**, *10*, 557−562.

(6) Holden, S. J.; Uphoff, S.; Kapanidis, A. N. DAOSTORM: An Algorithm for High-Density Super-Resolution Microscopy. *Nat. Methods* **2011**, *8*, 279−280.

(7) Leung, B. O.; Chou, K. C. Review of Super-Resolution Fluorescence Microscopy for Biology. *Appl. Spectrosc.* **2011**, *65*, 967−980.

(8) Park, K.-D.; Khatib, O.; Kravtsov, V.; Clark, G.; Xu, X.; Raschke, M. B. Hybrid Tip-Enhanced Nanospectroscopy and Nanoimaging of Monolayer WSe_2 with Local Strain Control. *Nano Lett.* **2016**, *16*, 2621−2627.

(9) Knoll, B.; Keilmann, F. Enhanced Dielectric Contrast in Scattering-Type Scanning Near-Field Optical Microscopy. *Opt. Commun.* **2000**, *182*, 321−328.

(10) Raschke, M. B.; Lienau, C. Apertureless Near-Field Optical Microscopy: Tip−Sample Coupling in Elastic Light Scattering. *Appl. Phys. Lett.* **2003**, *83*, 5089−5091.

(11) Novotny, L.; Hecht, B. *Principles of Nano-Optics*; Cambridge University Press: Cambridge, U.K., 2012.

(12) Park, K.-D.; Muller, E. A.; Kravtsov, V.; Sass, P. M.; Dreyer, J.; Atkin, J. M.; Raschke, M. B. Variable Temperature Tip-Enhanced Raman Spectroscopy of Single-Molecule Fluctuations and Dynamics. *Nano Lett.* **2016**, *16*, 479−487.

(13) Kravtsov, V.; Ulbricht, R.; Atkin, J. M.; Raschke, M. B. Plasmonic Nanofocused Four-Wave Mixing for Femtosecond Near-Field Imaging. *Nat. Nanotechnol.* **2016**, *11*, 459−464.

(14) Heu, C.; Berquand, A.; Elie-Caille, C.; Nicod, L. Glyphosate-Induced Stiffening of HaCaT Keratinocytes, a Peak Force Tapping Study on Living Cells. *J. Struct. Biol.* **2012**, *178*, 1−7.

(15) Novotny, L.; van Hulst, N. Antennas for Light. *Nat. Photonics* **2011**, *5*, 83−90.

(16) Zheng, X. T.; Li, C. M. Single Cell Analysis at the Nanoscale. *Chem. Soc. Rev.* **2012**, *41*, 2061−2071.

(17) Koopman, M.; Cambi, A.; de Bakker, B. I.; Joosten, B.; Figdor, C. G.; van Hulst, N. F.; Garcia-Parajo, M. F. Near-Field Scanning Optical Microscopy in Liquid for High Resolution Single Molecule Detection on Dendritic Cells. *FEBS Lett.* **2004**, *573*, 6−10.

(18) Höppener, C.; Novotny, L. Antenna-Based Optical Imaging of Single Ca^{2+} Transmembrane Proteins in Liquids. *Nano Lett.* **2008**, *8*, 642−646.

(19) van Zanten, T. S.; Lopez-Bosque, M. J.; Garcia-Parajo, M. F. Imaging Individual Proteins and Nanodomains on Intact Cell Membranes with a Probe-Based Optical Antenna. *Small* **2010**, *6*, 270−275.

(20) Schmid, T.; Yeo, B.-S.; Leong, G.; Stadler, J.; Zenobi, R. Performing Tip-Enhanced Raman Spectroscopy in Liquids. *J. Raman Spectrosc.* **2009**, *40*, 1392−1399.

(21) Zeng, Z.-C.; Huang, S.-C.; Wu, D.-Y.; Meng, L.-Y.; Li, M.-H.; Huang, T.-X.; Zhong, J.-H.; Wang, X.; Yang, Z.-L.; Ren, B. Electrochemical Tip-Enhanced Raman Spectroscopy. *J. Am. Chem. Soc.* **2015**, *137*, 11928−11931.

(22) Park, K.-D.; Park, D. J.; Lee, S. G.; Choi, G.; Kim, D.-S.; Byeon, C. C.; Choi, S. B.; Jeong, M. S. Operation of a Wet Near-Field Scanning Optical Microscope in Stable Zones by Minimizing the Resonance Change of Tuning Forks. *Nanotechnology* **2014**, *25*, 075704.

(23) Park, K.-D.; Kim, D.-C.; O, B-H.; Park, S.-G.; Lee, E.-H.; Lee, S. G. A New Method of Q Factor Optimization by Introducing Two Nodal Wedges in a Tuning-Fork/Fiber Probe Distance Sensor. *Rev. Sci. Instrum.* **2010**, *81*, 093702.

DOI: 10.1021/acs.jpcc.6b06563
J. Phys. Chem. C 2016, 120, 21138−21144

(24) Karrai, K.; Grober, R. D. Piezoelectric Tip-Sample Distance Control for Near Field Optical Microscopes. *Appl. Phys. Lett.* **1995**, *66*, 1842−1844.
(25) Morville, J.; Liu, J.; Callegari, A.; Chergui, M. Q-factor Optimization of a Tuning-Fork/Fiber Sensor for Shear-Force Detection. *Appl. Phys. Lett.* **2005**, *86*, 064103.
(26) Inman, D. J.; Singh, R. C. *Engineering Vibration*; Prentice Hall: Upper Saddle River, NJ, 2001; Vol. 3.
(27) Park, K.-D.; Lee, S. G.; Jeong, M. S. Epidermal Growth Factor Receptor Imaging of A431 Cancer Cells Using Gold Nanorods. *J. Nanosci. Nanotechnol.* **2011**, *11*, 7053−7056.
(28) Hayat, M. A. *Colloidal Gold: Principles, Methods, and Applications*; Elsevier: Amsterdam, 2012.
(29) Lewinski, N.; Colvin, V.; Drezek, R. Cytotoxicity of Nanoparticles. *Small* **2008**, *4*, 26−49.
(30) Höppener, C.; Siebrasse, J.; Peters, R.; Kubitscheck, U.; Naber, A. High-Resolution Near-Field Optical Imaging of Single Nuclear Pore Complexes under Physiological Conditions. *Biophys. J.* **2005**, *88*, 3681−3688.
(31) Haj, F. G.; Verveer, P. J.; Squire, A.; Neel, B. G.; Bastiaens, P. I. Imaging Sites of Receptor Dephosphorylation by PTP1B on the Surface of the Endoplasmic Reticulum. *Science* **2002**, *295*, 1708−1711.
(32) Maxfield, F. R.; Wüstner, D. Intracellular Cholesterol Transport. *J. Clin. Invest.* **2002**, *110*, 891−898.
(33) Hein, B.; Willig, K. I.; Hell, S. W. Stimulated Emission Depletion (STED) Nanoscopy of a Fluorescent Protein-Labeled Organelle inside a Living Cell. *Proc. Natl. Acad. Sci. U. S. A.* **2008**, *105*, 14271−14276.
(34) Rensen, W.; van Hulst, N.; Kämmer, S. Imaging Soft Samples in Liquid with Tuning Fork Based Shear Force Microscopy. *Appl. Phys. Lett.* **2000**, *77*, 1557−1559.
(35) Lee, L. F.; Schaller, R. D.; Haber, L. H.; Saykally, R. J. High Spatial Resolution Imaging with Near-Field Scanning Optical Microscopy in Liquids. *Anal. Chem.* **2001**, *73*, 5015−5019.
(36) Park, D. J.; Park, K.-D.; Choi, G. C.; Lee, S. G.; Byeon, C. C.; Jeong, M. S.; Choi, S. B. A Resonance Tracking Method for Stable Operation of a Near-Field Scanning Optical Microscope in Liquid Environment. *Curr. Appl. Phys.* **2014**, *14*, S12−S16.
(37) Koopman, M.; De Bakker, B.; Garcia-Parajo, M.; van Hulst, N. Shear Force Imaging of Soft Samples in Liquid Using a Diving Bell Concept. *Appl. Phys. Lett.* **2003**, *83*, 5083−5085.
(38) Manzo, C.; van Zanten, T. S.; Garcia-Parajo, M. F. Nanoscale Fluorescence Correlation Spectroscopy on Intact Living Cell Membranes with NSOM Probes. *Biophys. J.* **2011**, *100*, L8−L10.
(39) Bao, W.; Melli, M.; Caselli, N.; Riboli, F.; Wiersma, D.; Staffaroni, M.; Choo, H.; Ogletree, D.; Aloni, S.; Bokor, J.; et al. Mapping Local Charge Recombination Heterogeneity by Multidimensional Nanospectroscopic Imaging. *Science* **2012**, *338*, 1317−1321.
(40) Ianoul, A.; Grant, D. D.; Rouleau, Y.; Bani-Yaghoub, M.; Johnston, L. J.; Pezacki, J. P. Imaging Nanometer Domains of β-Adrenergic Receptor Complexes on the Surface of Cardiac Myocytes. *Nat. Chem. Biol.* **2005**, *1*, 196−202.
(41) Walker, K.-A. D.; Morgan, C.; Doak, S. H.; Dunstan, P. R. Quantum Dots for Multiplexed Detection and Characterisation of Prostate Cancer Cells Using a Scanning Near-Field Optical Microscope. *PLoS One* **2012**, *7*, e31592.
(42) Abulrob, A.; Lu, Z.; Baumann, E.; Vobornik, D.; Taylor, R.; Stanimirovic, D.; Johnston, L. J. Nanoscale Imaging of Epidermal Growth Factor Receptor Clustering Effects of Inhibitors. *J. Biol. Chem.* **2010**, *285*, 3145−3156.
(43) Gaffney, D. C.; Soyer, H. P.; Simpson, F. The Epidermal Growth Factor Receptor in Squamous Cell Carcinoma: An Emerging Drug Target. *Australas. J. Dermatol.* **2014**, *55*, 24−34.
(44) Galperin, E.; Verkhusha, V. V.; Sorkin, A. Three-Chromophore FRET Microscopy to Analyze Multiprotein Interactions in Living Cells. *Nat. Methods* **2004**, *1*, 209−217.
(45) Blakely, B. T.; Rossi, F. M.; Tillotson, B.; Palmer, M.; Estelles, A.; Blau, H. M. Epidermal Growth Factor Receptor Dimerization Monitored in Live Cells. *Nat. Biotechnol.* **2000**, *18*, 218−222.
(46) Park, K.-D.; Kim, Y. H.; Park, J.-H.; Park, J. S.; Lee, H. S.; Yim, S.-Y.; Lee, Y. H.; Jeong, M. S. Ultraviolet Tip-Enhanced Nanoscale Raman Imaging. *J. Raman Spectrosc.* **2012**, *43*, 1931−1934.
(47) Park, K.-D.; Jeong, H.; Kim, Y. H.; Yim, S.-Y.; Lee, H. S.; Suh, E.-K.; Jeong, M. S. Time-Resolved Ultraviolet Near-Field Scanning Optical Microscope for Characterizing Photoluminescence Lifetime of Light-Emitting Devices. *J. Nanosci. Nanotechnol.* **2013**, *13*, 1798−1801.
(48) Park, N.; Park, K.-D.; Chung, Y.; Jeong, M. S. Scanning Absorption Nanoscopy with Supercontinuum Light Sources Based on Photonic Crystal Fiber. *Rev. Sci. Instrum.* **2011**, *82*, 123102.

DOI: 10.1021/acs.jpcc.6b06563
J. Phys. Chem. C 2016, 120, 21138−21144